



# Erbium and praseodymium doped lithium tantalate electronic structure and metal-oxygen bonding analyses

Nicholas Dimakis<sup>a,f,\*</sup>, Andrea Pelayo Carvajal<sup>a,f</sup>, Mkhitar A. Hobosyan<sup>a,f</sup>,  
 Mohammed Jasim Uddin<sup>a,b,c,f</sup>, Tianna Resendez<sup>d</sup>, Yosef Herrera<sup>e</sup>, Karen S. Martirosyan<sup>a,f</sup>,  
 Muhammad I. Bhatti<sup>a</sup>, Constantine M. Tarawneh<sup>c</sup>

<sup>a</sup> Department of Physics and Astronomy, University of Texas Rio Grande Valley, Edinburg, TX 78539, USA

<sup>b</sup> Photonics and Energy Research Laboratory-PERL, UTRGV, Edinburg, TX 78539, USA

<sup>c</sup> Department of Mechanical Engineering, University of Texas Rio Grande Valley, Edinburg, TX 78539, USA

<sup>d</sup> Brownsville Early College High School, Brownsville, TX 78520, USA

<sup>e</sup> South Texas ISD Science Academy, Mercedes, TX 78570, USA

<sup>f</sup> Brownsville, TX 78500, USA

## ARTICLE INFO

### Keywords:

LiTaO<sub>3</sub>  
 Co-doping  
 DFT  
 QTAIM  
 ELF  
 Er<sup>+3</sup>  
 Pr<sup>+3</sup>

## ABSTRACT

Electronic information and optical properties coupled with the Quantum Theory of Atoms in Molecules (QTAIM) and Electron Localization Function (ELF) analyses are used to elucidate the erbium (Er<sup>+3</sup>) and praseodymium (Pr<sup>+3</sup>) intraband f-f transitions in the lithium tantalate (LiTaO<sub>3</sub>) doped and co-doped configurations and the metal-oxygen bonding. The generalized gradient approximation calculations show that the Er<sup>+3</sup>- and Pr<sup>+3</sup>-4f bands appear closer to the conduction band bottom for Er<sup>+3</sup> and Pr<sup>+3</sup> at the Li sites and to the valence band top for Er<sup>+3</sup> at the Ta sites. However, the corresponding hybrid functional calculations for the dopants at the Li site show that the Er<sup>+3</sup> and Pr<sup>+3</sup>-4f bands spread in energy, which agrees with the observed intraband f-f transitions from the optical properties calculations. QTAIM shows that Ta-, Er<sup>+3</sup>-, and Pr<sup>+3</sup>-O bonding is incipient covalent for all configurations of this work. The absence of ELF in the metal-O regions aligns with QTAIM on the lack of strong covalent bonding in these compounds. This complementary insight highlights how weakly interacting metal-O atoms lead to delocalized electron density, a feature that influences the physical, electronic, and chemical behavior of the LiTaO<sub>3</sub>.

## 1. Introduction

Lithium tantalate (LiTaO<sub>3</sub>; LT) is a strong ferroelectric material that has garnered significant interest due to its unique optical, acoustical, and electronic properties with a wide range of applications. It has the perovskite structure ABX<sub>3</sub>, where A is an alkali atom, B is a transition metal atom, and X is an oxygen or a halide atom [1]. Various synthesis methods, such as hydrothermal and solvothermal processes, produce pure-phase LT [2,3]. The LT thermodynamic stability has been examined, revealing insights into their formation enthalpies and structural properties [4]. Moreover, LT has been extensively researched for its piezoelectric properties. It is suitable for applications in high-frequency components, acoustic wave devices, and optical modulators with spontaneous polarization, which an electric field can reverse [5,6]. Furthermore, LT-modified piezoceramics have demonstrated enhanced

electromechanical properties [5]. It has also shown promise in optical applications, such as optical parametric generation and chirped pulse amplification [6,7]. With a Curie temperature of about 600°C, LT is more stable than similar perovskite materials like lithium niobate. Thus, LT is suitable for high-temperature environments requiring stable ferroelectric and piezoelectric properties. The breadth of research on LT highlights its versatility and potential across various technological fields, from materials science to optics and beyond.

The doping and co-doping of LT with lanthanides, such as LT doped with Er<sup>+3</sup> (LT: Er<sup>+3</sup>) [8–10], Pr<sup>+3</sup> (LT: Pr<sup>+3</sup>) [11], Ce<sup>+3</sup> [12], La<sup>+3</sup> [13], and co-doped with Pr<sup>+3</sup> and Gd<sup>+3</sup> [14] and Er<sup>+3</sup> with Yb<sup>+3</sup> [15] have garnered significant interest due to their unique optical properties. Shi et al. stated that the LT: Er<sup>+3</sup> combines the lasing properties of Er<sup>+3</sup> with the nonlinear optical properties of the host LT [15]. This statement can be extended to LT doping with other lanthanides. Yang et al. reported

\* Corresponding author at: Department of Physics and Astronomy, University of Texas Rio Grande Valley, Edinburg, TX 78539, USA.

E-mail address: [nicholas.dimakis@utrgv.edu](mailto:nicholas.dimakis@utrgv.edu) (N. Dimakis).

LT: Er<sup>+3</sup> emission spectra with the Er<sup>+3</sup>-4f intraband assignments for samples synthesized using the molten salt method [9] and the solid combustion route [8]. Qui et al. found that LT: Pr<sup>+3</sup> has intense piezoluminescence by measuring the piezoluminescence spectra, whereas Ismangil et al., for LT doped with Ce<sup>+3</sup>, reported changes in the bandgap energy due to temperature variations [12]. Irzaman et al. showed that increased La<sup>+3</sup> concentration lowers the bandgap and increases the refractive index for LT-doped La<sup>+3</sup> thin films [13]. Co-doping LT with Pr<sup>+3</sup> and Gd<sup>+3</sup> led to increased mechanoluminescence and photostimulated luminescence [14], whereas co-doping Er<sup>+3</sup> with Yb<sup>+3</sup> led to upconversion emission tuning from green to red [15]. Co-doping LT with Er<sup>+3</sup> and Pr<sup>+3</sup> can result in new emission peaks in the visible and near IR, resulting in more versatile photoluminescent material that can be used in NIR detectors with specific applications in laser triangulation for distance measurements [16].

Density functional theory (DFT) [17,18] and the GW approximation [19,20] have been used to calculate the LT band structure [10,21–25]. The LT bandgap is indirect and in the 3.71–5.58 eV [23,26–30] range. The GW approximation includes quasiparticle energy calculations (i.e., excitation spectra) by incorporating many-body effects in the *e-e* interaction [31]. Although GW is superior to DFT for electronic and optical properties calculations, it does not include *e-h* interactions, and it is limited to small supercells due to significant RAM requirements. DFT calculations on perovskite doping have been reported. Brahim et al. reported changes in the electronic and optical properties of the LiNbO<sub>3</sub> due to chalcogen doping [32]. Obodo et al. studied the changes in the ZnTiO<sub>3</sub> properties due to doping and co-doping with Yb<sup>+3</sup>, Ho<sup>+3</sup>, Tm<sup>+3</sup>, and Er<sup>+3</sup> [33]. Ouyang et al. studied the changes in the cesium lead halide perovskite (CsPbX<sub>3</sub>, X = Cl, Br, and I) due to doping with Yb<sup>+3</sup> and Er<sup>+3</sup> experimentally via photoluminescence and computationally using DFT. We have reported changes in the electronic and optical properties by doping LT with 4.167 mol% Er<sup>+3</sup> using DFT [10]. Our experiments have complemented these DFT results. However, we are unaware of other computational studies on LT doped with Er<sup>+3</sup> and/or Pr<sup>+3</sup>.

The Quantum Theory of Atoms in Molecules (QTAIM), developed by Richard Bader [34,35], is a powerful framework for analyzing chemical bonding. QTAIM uses the topology of the electron density  $\rho(\vec{r})$ ,  $\nabla\rho(\vec{r})$ , and the Laplacian  $\nabla^2\rho(\vec{r})$  to describe atoms and their bonding [36]. It allows for the quantum mechanical definition of molecular structures, enabling a detailed analysis of various types of interactions, including covalent bonds, non-covalent interactions, and the nature of chemical bonds [37]. In QTAIM,  $\nabla\rho(\vec{r}) = 0$  at critical points. There are four types of critical points based on the number and nature of non-zero eigenvalues of the Hessian matrix for  $\rho(\vec{r})$ . Here, we will focus on the bond critical points (3, -1), where “3” stands for the number of the Hessian eigenvalues and “-1” for the algebraic summation of positive and negative eigenvalues. The bond critical point appears as a saddle point in the  $\rho(\vec{r})$  and is a necessary condition for bonding between two atoms. There are several approaches for classifying interatomic interactions using QTAIM [38–41]. It must be emphasized that adopting a single criterion to define a bonding in crystals is challenging since, in several cases, ionic, covalent, metallic, and van der Waals-like interactions are simultaneously present [41,42]. QTAIM has been used to analyze the nature and behavior of the Rb-O and U-O bonds on the perovskite RbUO<sub>3</sub> [43].

The Electron Localization Function (ELF) describes the localization of electrons in molecules and solids and analyzes the nature of the chemical bond. Becke and Edgecombe introduced the ELF as a one-electron density function to characterize bonded and nonbonded regions within molecules [44]. This function is based on a topological analysis of local quantum mechanical functions related to the Pauli exclusion principle, making it a robust descriptor of chemical bonding [45]. QTAIM and ELF are functional and basis-set independent approaches, which enhance the validity of their results [46,47]. ELF

analysis has been reported on perovskites. Feng et al. used ELF to show that Pb atoms are unbonded on the surface of the methylammonium lead iodide perovskite [48]. Fang et al. used ELF analysis to examine how lone-pair electrons of Bi and Pb break the inversion symmetry in the BiPbTi<sub>2</sub>O<sub>6</sub> perovskite [49].

Here, we use periodic DFT to analyze the electronic and optical properties of LT doped and co-doped with Er<sup>+3</sup> and Pr<sup>+3</sup>. We have selected Pr<sup>+3</sup> as the co-doping element due to having more 4 f vacancies than Er<sup>+3</sup> (i.e., 4 f<sup>3</sup>6 s<sup>2</sup> is the valence electron configuration for isolated Pr) and thus is expected to produce stronger f-f intraband transitions. The band structure and the densities-of-states (DOS) are calculated using the generalized gradient approximation (GGA) and the HSE06 hybrid functional. HSE06 calculations are computationally expensive in terms of RAM and CPU demand. However, they improve the 4 f band locations in the energy relative to the GGA [10]. We use QTAIM and ELF to analyze the Li and Ta bonding with O and the bonding of Er<sup>+3</sup> and Pr<sup>+3</sup> with O.

## 2. Computational methods

### 2.1. Supercell modeling, DFT parameters, and optical properties

The supercell used here for the LT-doped and co-doped configurations with Er<sup>+3</sup> and Pr<sup>+3</sup> is the same as in our last reports [10,50,51]. Fig. 1 shows the LT 2 × 2 × 1 supercell (space group R3c), with 24 Li, 24 Ta, and 72 O atoms (120 atoms in total). In the doped configurations, the Er<sup>+3</sup> and Pr<sup>+3</sup> atoms occupy either the Li or the Ta site, whereas, for the Er<sup>+3</sup>-Pr<sup>+3</sup> co-doped configuration, both dopants occupy Li sites. The supercells were optimized using the lanthanides 4 f orbitals in the core. We could not obtain optimized geometries and conformational energies for co-doped configurations with Er<sup>+3</sup> and Pr<sup>+3</sup> in the Ta site and Er<sup>+3</sup> concurrently in the Li and Ta sites. The co-doping configurations with Er<sup>+3</sup> and Pr<sup>+3</sup> located at either the Li or the Ta site or both at the Ta site will be examined in future work.

The details of the DFT parameters used to calculate the optimal geometries, the electronic information, and the optical properties can be found in Ref. [10]. In brief, we used the periodic code Vienna *Ab initio* Simulation Package (VASP) [52–55] to solve the DFT Kohn-Sham equations under the Perdew–Burke–Ernzerhof (PBE) functional [56] paired with the projector augmented-wave (PAW) pseudopotentials [57, 58]. Van der Waals interactions were considered via the D3 semi-empirical correction by Grimme [59]. Electronic information was also obtained using the HSE06 hybrid functional for bandgap improvement [60–64] and the locations in energy for the 4 f valance orbitals [10]. We used the  $\Gamma$ -centered 6 × 6 × 6 BZ grid for sampling the Brillouin-zone (BZ) for all calculations except for the QTAIM, atom charges, and ELF, where the BZ was only sampled at the  $\Gamma$  point. Bader atomic charges and volumes were calculated using the Bader Charge Analysis code by Henkelman and co-workers [65–68]. VASP calculates the frequency-dependent dielectric function  $\varepsilon(\omega) = \varepsilon_R(\omega) + i\varepsilon_I(\omega)$ , where  $\varepsilon_R(\omega)$  and  $\varepsilon_I(\omega)$  are the real and imaginary parts, respectively, as follows: First, it calculates the imaginary part from [69],

$$\varepsilon_I^{ij}(\omega) \propto \sum_{c,v} \sum_k \langle U_{ck} | p_i | U_{vk} \rangle \langle U_{ck} | p_j | U_{vk} \rangle \delta(\omega_{ck}(k) - \omega_{vk}(k) - \omega) \quad (1)$$

for  $i, j = x, y, z$ , the summation is over the valance bands  $v$  and the conduction bands  $c$ ,  $p$  is the momentum operator, and  $|U_{lk}\rangle$ ,  $l = v, c$  is the crystal wavefunction. Second, the real part is calculated using the Kramers-Kronig relation  $\varepsilon_R(\omega) = 1 + \frac{2}{\pi} \int_0^\omega \frac{\omega_1 \varepsilon_I(\omega_1) d\omega_1}{\omega_1^2 - \omega^2}$ . The frequency-dependent refractive index  $n(\omega)$  and extinction coefficient  $k(\omega)$  are written in terms of  $\varepsilon_R(\omega)$  and  $\varepsilon_I(\omega)$  as follows:

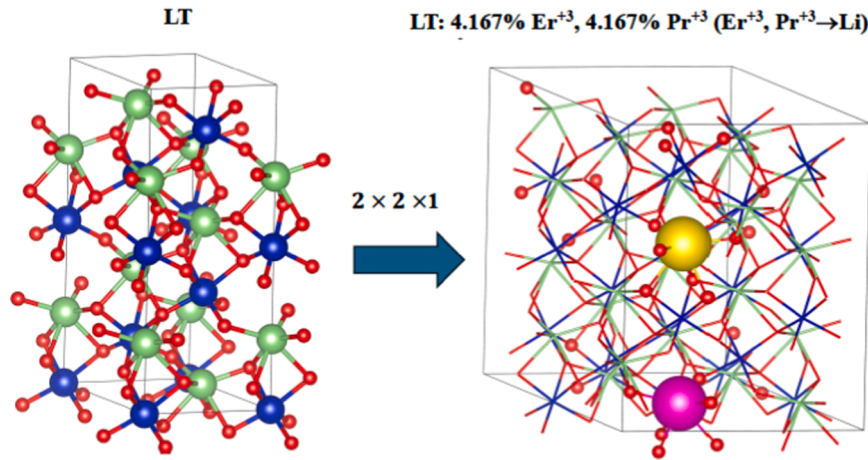


**Fig. 1.** Left. The  $\text{LiTaO}_3$  (LT) unit cell. Right. The  $2 \times 2 \times 1$  supercell of the LT: 4.167 %  $\text{Er}^{+3}$ , 4.167 %  $\text{Pr}^{+3}$  with  $\text{Pr}^{+3}$  and  $\text{Er}^{+3}$  at the Li site ( $\text{Er}^{+3}$ ,  $\text{Pr}^{+3} \rightarrow \text{Li}$ ). Atoms are colors as follows: Li, green; Ta, blue;  $\text{Pr}^{+3}$ , yellow;  $\text{Er}^{+3}$ , magenta; O, red. The thin black lines denote the supercell boundaries.

$$n(\omega) = \left( \frac{[\epsilon_R(\omega)^2 + \epsilon_I(\omega)^2]^{\frac{1}{2}} + \epsilon_R(\omega)}{2} \right)^{\frac{1}{2}}, \quad (2)$$

$$R(\omega) = \frac{(n(\omega) - 1)^2 + k(\omega)^2}{(n(\omega) + 1)^2 + k(\omega)^2}. \quad (4)$$

$$k(\omega) = \left( \frac{[\epsilon_R(\omega)^2 + \epsilon_I(\omega)^2]^{\frac{1}{2}} - \epsilon_R(\omega)}{2} \right)^{\frac{1}{2}}, \quad (3)$$

### 2.2. QTAIM and ELF parameters

QTAIM and ELF are calculated using the Critic2 code [70,71], which reads VASP output. Fig. 2a shows the QTAIM molecular graph for the LT:4.176 %  $\text{Er}^{+3}$ , 4.176 %  $\text{Pr}^{+3}$ , which is a collection of  $\nabla\rho(\vec{r})$  trajectories originating at the  $(3, -1)$  bond critical points and connecting the electron density critical points maxima  $(3, -3)$  with other maxima [72]. Fig. 2b shows the negative of the Laplacian of the electron density at the

The frequency-dependent reflectivity  $R(\omega)$  is written in terms of  $n(\omega)$ , and  $k(\omega)$  as

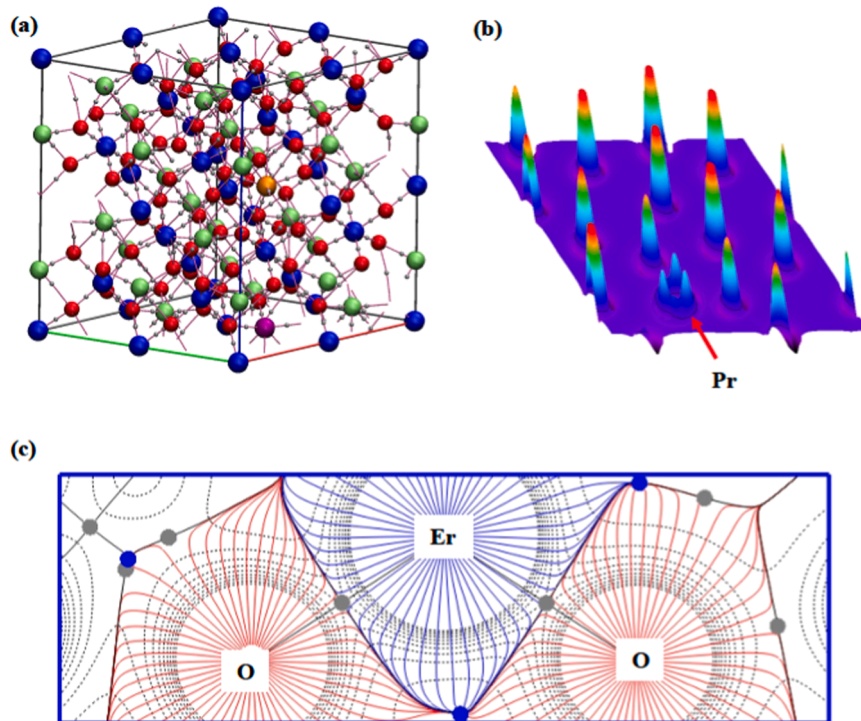


**Fig. 2.** (a) The molecular graph of the electron density for the optimized LT:4.176 %  $\text{Er}^{+3}$ , 4.176 %  $\text{Pr}^{+3}$  supercell using VMD and Critic2. Only the  $(3, -1)$  bond critical points are shown. Atoms are colors as follows: Ta, blue; O, red; Li, green;  $\text{Er}^{+3}$ , purple;  $\text{Pr}^{+3}$ , orange. Small gray spheres show bond critical points. (b) The negative of the Laplacian of the electron density ( $-\nabla^2\rho(\vec{r})$ ) at the  $(0 0 1)$  plane, which includes the  $\text{Pr}^{+3}$  atom, whereas the remaining peaks are from oxygens (generated via AIM-UC [73]). (c) The contour plot of the electron density along the plane defined by  $\text{Er}^{+3}$  and two nearby O atoms. Blue and gray circles represent  $(3, +3)$  and  $(3, -1)$  critical points, respectively. The trajectories are blue and red for the  $\text{Er}^{+3}$  and O basins, respectively.

(001) plane at the  $\text{Pr}^{+3}$  c-axis location, and Fig. 2c shows the contour plot of electron density along the plane defined by  $\text{Er}^{+3}$  and two nearby O atoms, as well as the atomic basins and the trajectories. The atomic basins are regions of space traversed by  $\nabla\rho(\vec{r})$  and bounded by zero-flux surfaces.

QTAIM can be used to characterize the nature of a chemical bond via the adimensional ratio ( $|V_b|/G_b$ ) at the bond critical point  $b$ , where  $V$  and  $G$  are the potential and the definite kinetic energies, respectively [38, 41]. Espinosa et al. stated that for  $|V_b|/G_b > 2$  the interaction between two atoms is of a shared shell (i.e., covalent bonding), whereas for  $|V_b|/G_b < 1$  is of a closed shell [33]. For  $1 < |V_b|/G_b < 2$ , this interaction indicates an incipient covalent bond formation. Closed shell interactions are expected to have  $H_b = V_b + G_b > 0$  and  $\nabla^2\rho_b(\vec{r}) > 0$ , whereas the opposite is expected for shared shell interactions.

ELF  $\eta(\vec{r})$  measures the electron localization in atomic and molecular systems. It was originally described by Becke and Edgecombe [44] as  $\eta(\vec{r}) = 1/(1 + \chi(\vec{r})^2)$ , where  $\chi(\vec{r})$  is the ELF kernel and  $0 \leq \eta(\vec{r}) \leq 1$ . The case of  $\eta(\vec{r}) = 1$  corresponds to perfect localization, whereas  $\eta(\vec{r}) = 0.5$  to the electron gas case.

### 3. Results and discussion

#### 3.1. DFT calculated structural information for LT-doped and co-doped configurations

Table 1 shows the lattice parameters and the metal-O distances for this work's doped and co-doped configurations. We also include the LT structural information from our previous report for comparison. Doping LT with  $\text{Er}^{+3}$  and  $\text{Pr}^{+3}$  affects the  $a$  and  $c$  supercell parameters and the metal-O distances. Specifically, the  $a$  parameter increases upon doping with  $\text{Er}^{+3}$  and  $\text{Pr}^{+3}$ , whereas the  $c$  parameter increases for all doped cases except for LT: 4.167 %  $\text{Pr}^{+3}$  with  $\text{Pr}^{+3}$  at the Li site and for the co-doped configuration. Moreover, there is an analogous relationship between the  $a$  and  $c$  parameters and the  $\text{Er}^{+3}$  doping (for  $\text{Er}^{+3}$  in the Li site, LT: 8.334 %  $\text{Er}^{+3}$ ,  $a \sim 10.44 \text{ \AA}$  from Table 1; LT: 4.167 %  $\text{Er}^{+3}$ ,  $a \sim 10.36 \text{ \AA}$  from Ref. [10]). Doping LT with  $\text{Er}^{+3}$  and  $\text{Pr}^{+3}$  leads to Li-O elongation for all cases except when the dopants concentration is 4.167 % and are in the Ta site and for the co-doped configuration

**Table 1**

Lattice parameters and metal-oxygen interatomic distances for LT, LT: 4.167 %  $\text{Pr}^{+3}$ , LT: 8.334 %  $\text{Er}^{+3}$ , and LT: 4.167 %  $\text{Er}^{+3}$ , 4.167 %  $\text{Pr}^{+3}$ . For the doped and co-doped configurations, the Li-O and Ta-O distances refer to atoms further away from the  $\text{Er}^{+3}$  site in the supercell.

Structure	Lattice parameters		Metal-O distances			
	$a$ (=b) ( $\text{\AA}$ )	$c$	Li-O	Ta-O	$\text{Er}^{+3}$ - O	$\text{Pr}^{+3}$ - O
LT <sup>a</sup>	10.29667	13.84594	2.021	1.929		
LT: 4.167 % $\text{Pr}^{+3}$ ( $\text{Pr}^{+3} \rightarrow \text{Li}$ )	10.39261	13.80889	2.311	2.068		2.709
			2.401	2.054		2.671
					2.025	1.942
LT: 4.167 % $\text{Pr}^{+3}$ ( $\text{Pr}^{+3} \rightarrow \text{Ta}$ )	10.31718	13.88754	2.320	2.068		2.178
			2.015	1.928		2.094
LT: 8.334 % $\text{Er}^{+3}$ ( $\text{Er}^{+3} \rightarrow \text{Li}$ )	10.43830	13.85538	2.357	2.041	2.365	
			2.024	1.960	2.156	
LT: 8.334 % $\text{Er}^{+3}$ ( $\text{Er}^{+3} \rightarrow \text{Ta}$ )	10.35484	13.99346	2.315	2.031	2.237	
			2.028	1.943	2.216	
					2.192	
					2.167	
					2.150	
LT: 4.167 % $\text{Er}^{+3}$ , 4.167 % $\text{Pr}^{+3}$ ( $\text{Er}^{+3}$ , $\text{Pr}^{+3} \rightarrow$ Li)	10.44188	13.82303	2.308	2.053	2.422	2.598
			2.037	1.941	2.225	2.243

<sup>a</sup> From Ref. [10].

(Table 1 and Ref. [51]). In the former cases, the shortest Li-O distance is decreased due to doping, whereas co-doping LT with  $\text{Er}^{+3}$  and  $\text{Pr}^{+3}$  decreases the longer of the Li-O distances.

The LT, LT doped, and co-doped configurations have each metal atom coordinated with six oxygens in an octahedral symmetry. This symmetry is distorted, and three oxygens are located at different metal-O distances than the other three (Table 1). However, additional distortions are evidenced in the lanthanide-O distances for LT: 4.167 %  $\text{Pr}^{+3}$  with  $\text{Pr}^{+3}$  at the Li site and for the LT: 8.334 %  $\text{Er}^{+3}$  with  $\text{Er}^{+3}$  at the Ta site configuration ( $d_{\text{Er}^{+3}-\text{O}} = 5.17 \text{ \AA}$ ). Crystal field theory [74] states that lattice distortions break band degeneracies and lead to their splitting. Wu et al. reported that lattice distortions on  $(\text{Ca}_{1-x}\text{Eu}_x)\text{WO}_4$  ( $x = 0-21 \text{ mol\%}$ ) phosphors affected the intrinsic luminescence of the matrix and the f-f excitation transitions of the  $\text{Eu}^{3+}$  activators [75]. Table 1 shows that, for the latter case, the  $\text{Er}^{+3}$ -O distortions are significant. They are responsible for this configuration's enhanced f-f intraband transitions, which are not observed in any other doped case with  $\text{Er}^{+3}$  or  $\text{Pr}^{+3}$  at the Ta site (vide infra).

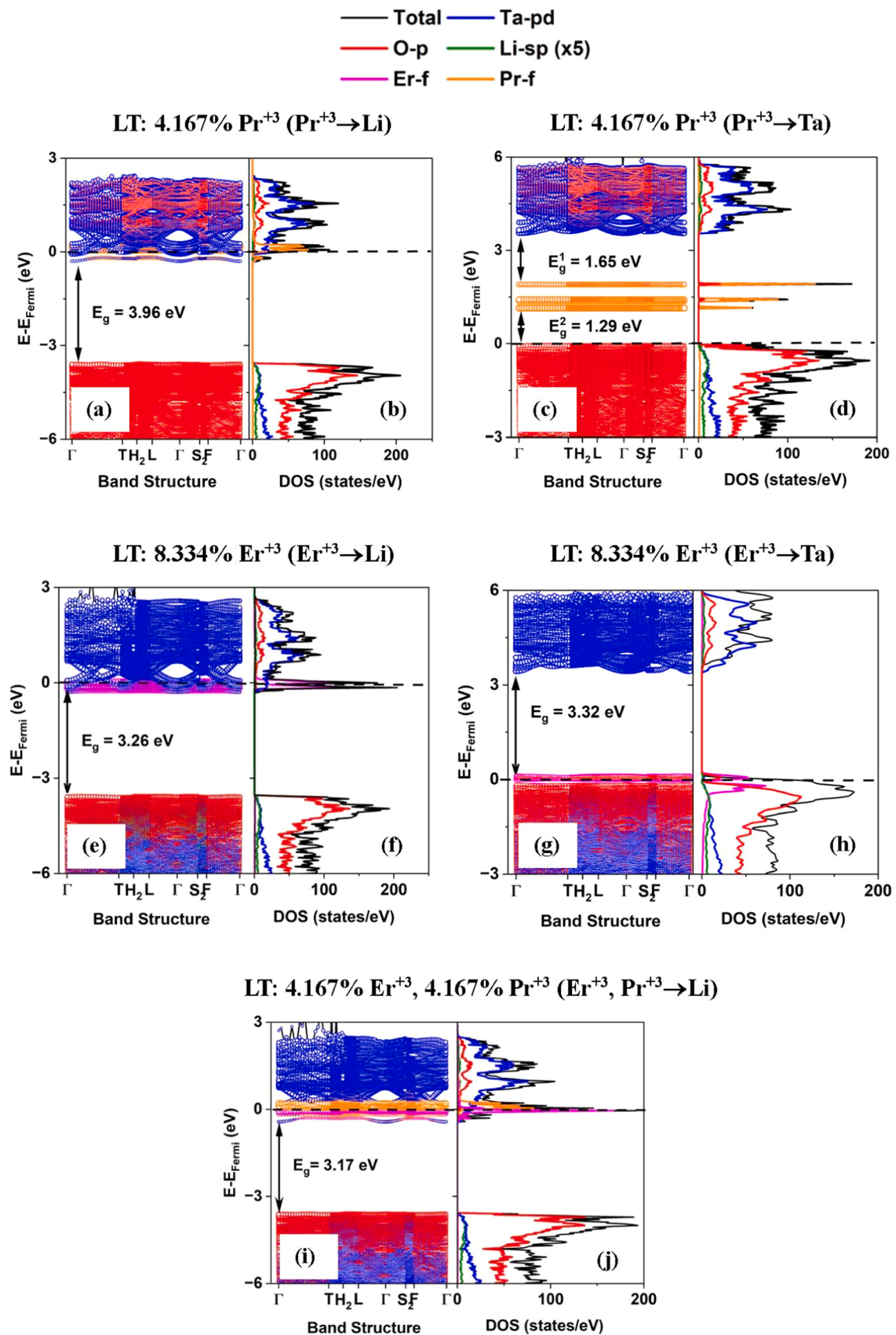
#### 3.2. Band structure and densities of states (DOS) calculations

Fig. 3 shows the electronic band structure with orbital projections and the corresponding total and projected DOS per orbital using the PBE functional for this work's doped and co-doped configurations. Fig. 4 shows the same information as Fig. 3 using the HSE06 functional, except for the LT: 8.334 %  $\text{Er}^{+3}$  with  $\text{Er}^{+3}$  at the Ta site. The HSE06 calculated electronic information is unavailable for this configuration due to the computational recourses needed. For all configurations here, the valance band is dominated by O-p orbitals and the conduction band by the Ta-pd orbitals. The DOS shows some mixing of the Ta-pd orbitals with O-p orbitals in the valance band, whereas the Li orbitals contribution in the DOS is small. The mixing of the Ta-pd with O-p orbitals is indicative of Ta-O covalent bonding. However, its strength cannot be determined by DOS.

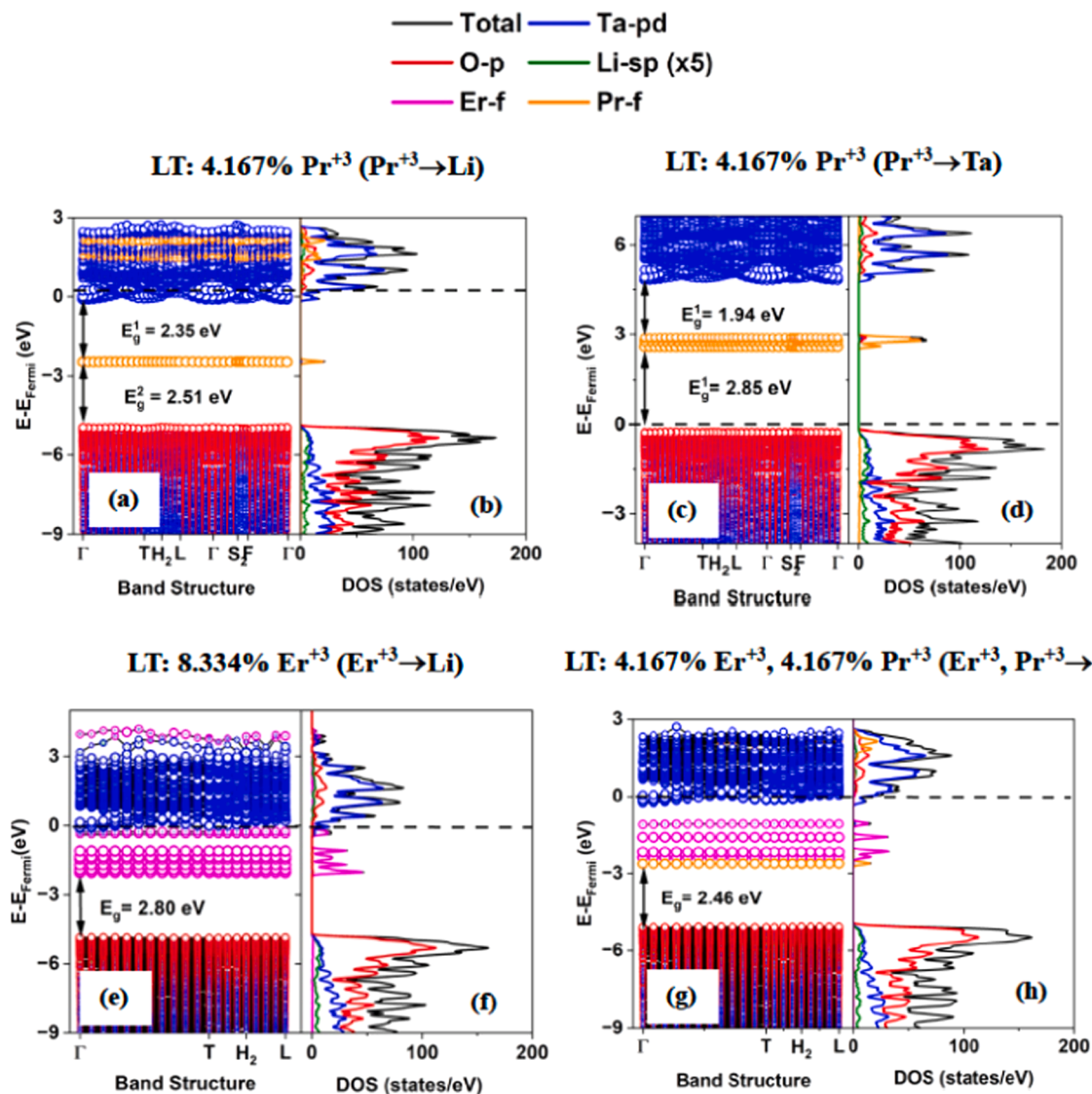
The PBE band structure calculations show that the  $\text{Er}^{+3}$ - and  $\text{Pr}^{+3}$ -4f bands are located at the conduction band bottom when  $\text{Er}^{+3}$  and  $\text{Pr}^{+3}$  are at the Li site, which agrees with our past report for LT: 4.167 %  $\text{Er}^{+3}$  [10]. However, there are major differences in the location of the lanthanide 4 f bands using the PBE functional when  $\text{Er}^{+3}$  and  $\text{Pr}^{+3}$  are in the Ta site relative to the Li site. In the former case, the  $\text{Er}^{+3}$ -4f bands are found at the valance band top, whereas in the latter case, the  $\text{Pr}^{+3}$ -4f bands split, are in the bandgap, and above the Fermi energy, thus empty. The intraband f-f transitions are favored when the 4 f bands are partially occupied, which is not the case for the doped configuration with  $\text{Pr}^{+3}$  at the Ta site. The PBE calculated bandgaps for LT:  $\text{Er}^{+3}$  at 4.167 % and 8.334 % doping decrease along with the increase of  $\text{Er}^{+3}$  doping if  $\text{Er}^{+3}$  is at the Li site, whereas the opposite is observed for the configurations with  $\text{Er}^{+3}$  is at the Ta site. Specifically, for the doped configurations with  $\text{Er}^{+3}$  at the Li site, the bandgaps are 3.42 eV and 3.49 eV, respectively, for 4.167 % and 8.334 % mol  $\text{Er}^{+3}$ . However, for  $\text{Er}^{+3}$  at the Ta site, these bandgaps are 3.05 eV and 3.32 eV, respectively.

Fig. 3h shows the DOS for the LT: 8.334 %  $\text{Er}^{+3}$  with  $\text{Er}^{+3}$  at the Ta site. Recall that this configuration shows additional distortions to the  $\text{Er}^{+3}$ -O distances. When  $\text{Er}^{+3}$  is at the Ta site, increased doping broadens Er-4f bands and upshifts them relative to the lower concentration configuration (Supplementary Material, Fig. S1). The latter increases the Er-4f vacancies, leading to stronger f-f intraband transitions.

As expected, the HSE06 calculations show larger bandgaps than the PBE calculations for the same configurations. Moreover, these calculations show that for the doped and co-doped configurations with the dopant at the Li site, the 4 f orbitals are broadened in energy and some are located in the bandgap and below the Fermi energy, thus not empty. However, for  $\text{Pr}^{+3}$  at the Ta site, the  $\text{Pr}^{+3}$ -4f appear compacted and are located in the bandgap, as in the PBE calculation. Although these calculations are computationally expensive, they provide an improved description of the bandgap and the location of the lanthanide 4f orbitals.



**Fig. 3.** Electronic band structure with orbital projections (a, c, e, g, and i) and corresponding total and projected DOS per orbital (b, d, f, h, and j) using the PBE calculations for LT: 4.167 % Pr<sup>+3</sup> with Pr<sup>+3</sup> at the Li site (Pr<sup>+3</sup>→ Li; a and b), LT: 4.167 % Pr<sup>+3</sup> with Pr<sup>+3</sup> at the Ta site (Pr<sup>+3</sup>→ Ta; c and d), LT: 8.334 % Er<sup>+3</sup> with Er<sup>+3</sup> at the Li site (Er<sup>+3</sup>→ Li; e and f), LT: 8.334 % Er<sup>+3</sup> with Er<sup>+3</sup> at the Ta site (Er<sup>+3</sup>→ Ta; g and h), and LT: 4.167 % Er<sup>+3</sup>, 4.167 % Pr<sup>+3</sup> with Pr<sup>+3</sup> and Er<sup>+3</sup> at the Li site (Er<sup>+3</sup>, Pr<sup>+3</sup>→ Li; i and j). The dashed horizontal line is the Fermi energy ( $E_{Fermi}$ ).



**Fig. 4.** Electronic band structure with orbital projections (a, c, e, g, and i) and corresponding total and projected DOS per orbital (b, d, f, h, and j) using the HSE06 calculations for LT: 4.167 %  $\text{Pr}^{+3}$  with  $\text{Pr}^{+3}$  at the Li site ( $\text{Pr}^{+3} \rightarrow \text{Li}$ ; a and b), LT: 4.167 %  $\text{Pr}^{+3}$  with  $\text{Pr}^{+3}$  at the Ta site ( $\text{Pr}^{+3} \rightarrow \text{Ta}$ ; c and d), LT: 8.334 %  $\text{Er}^{+3}$  with  $\text{Er}^{+3}$  at the Li site ( $\text{Er}^{+3} \rightarrow \text{Li}$ ; e and f), LT: 4.167 %  $\text{Er}^{+3}$ , 4.167 %  $\text{Pr}^{+3}$  with  $\text{Pr}^{+3}$  and  $\text{Er}^{+3}$  at the Li site ( $\text{Er}^{+3} \rightarrow \text{Ta}$ ; g and h). The dashed horizontal line is the Fermi energy ( $E_{\text{Fermi}}$ ).

The latter can be used for an accurate description of the  $f$ - $f$  transition assignments and comparison with photoluminescence data, as in our past work.

### 3.3. Optical properties calculations

Fig. 5. shows the frequency-dependent dielectric function imaginary and real parts  $\epsilon_I$  and  $\epsilon_R$  for LT and its  $\text{Er}^{+3}$  and  $\text{Pr}^{+3}$  doped and co-doped counterparts, as well as the refractive index  $n$ , and the reflectivity  $R$ . The frequency-dependent dielectric function real part  $\epsilon_R$  and the refractive index  $n$  curves are similar. The peaks in the imaginary part of the dielectric function  $\epsilon_I$  are indicative of transitions from the valance band to the conduction band (interband), as well as for transitions within the same band (intra-band). There is an analogous relationship between  $\epsilon_I$  peak values and the transition strength (Eq. 1). Here, we will focus on changes in the  $\epsilon_I$  within the bandgap since the  $\epsilon_I$  peaks outside of the bandgap refer to transitions within the LT bands. Our calculated optical properties use the independent particle approximation (IPA) [76], which does not consider  $e$ - $h$  interactions. Moreover, using the GGA for these calculations does not allow intra-band  $f$ - $f$  transitions to be resolved

as multiple peaks in the frequency-dependent dielectric function, as in the photoluminescence spectra. However, our optical properties could serve as a comparison tool for an overall  $f$ - $f$  transition strength among the doped configurations of this work.

Fig. 5a shows several  $\epsilon_I$  peaks in the bandgap at about 0.25–0.5 eV, corresponding to  $\text{Er}^{+3}$  and  $\text{Pr}^{+3}$  intra-band  $f$ - $f$  transitions. For LT: 4.167 %  $\text{Pr}^{+3}$  with  $\text{Pr}^{+3}$  at the Ta site, no such peak is observed for  $\epsilon$ ,  $n$ , and  $R$ , which agrees with the presence of the  $\text{Pr}^{+3}$ -4f bands in the bandgap above the Fermi energy and thus unpopulated. In the energy region of 0.25–0.5 eV, the highest  $\epsilon_I$  peak is observed for the co-doped configuration LT: 4.167 %  $\text{Er}^{+3}$ , 4.167 %  $\text{Pr}^{+3}$  followed by LT: 4.167 %  $\text{Pr}^{+3}$  with the dopants at the Li site, and in turn by LT: 8.334 %  $\text{Er}^{+3}$  with the dopants at either the Li or the Ta site. The doping of LT with  $\text{Pr}^{+3}$  strengthens the intra-band  $f$ - $f$  transitions relative to configurations containing only  $\text{Er}^{+3}$  due to the increased vacancies in the  $\text{Pr}^{+3}$ -4f bands relative to  $\text{Er}^{+3}$ -4f. Recall that for the isolated  $\text{Pr}^{+3}$  and  $\text{Er}^{+3}$  ions, the  $\text{Pr}^{+3}$ -4f orbital has 2 electrons, and the  $\text{Er}^{+3}$ -4f orbital has 11 electrons. Moreover, for LT:  $\text{Er}^{+3}$ , there is an analogous relationship between the  $\epsilon_I$  peak value at the above energy region and the  $\text{Er}^{+3}$  doping.

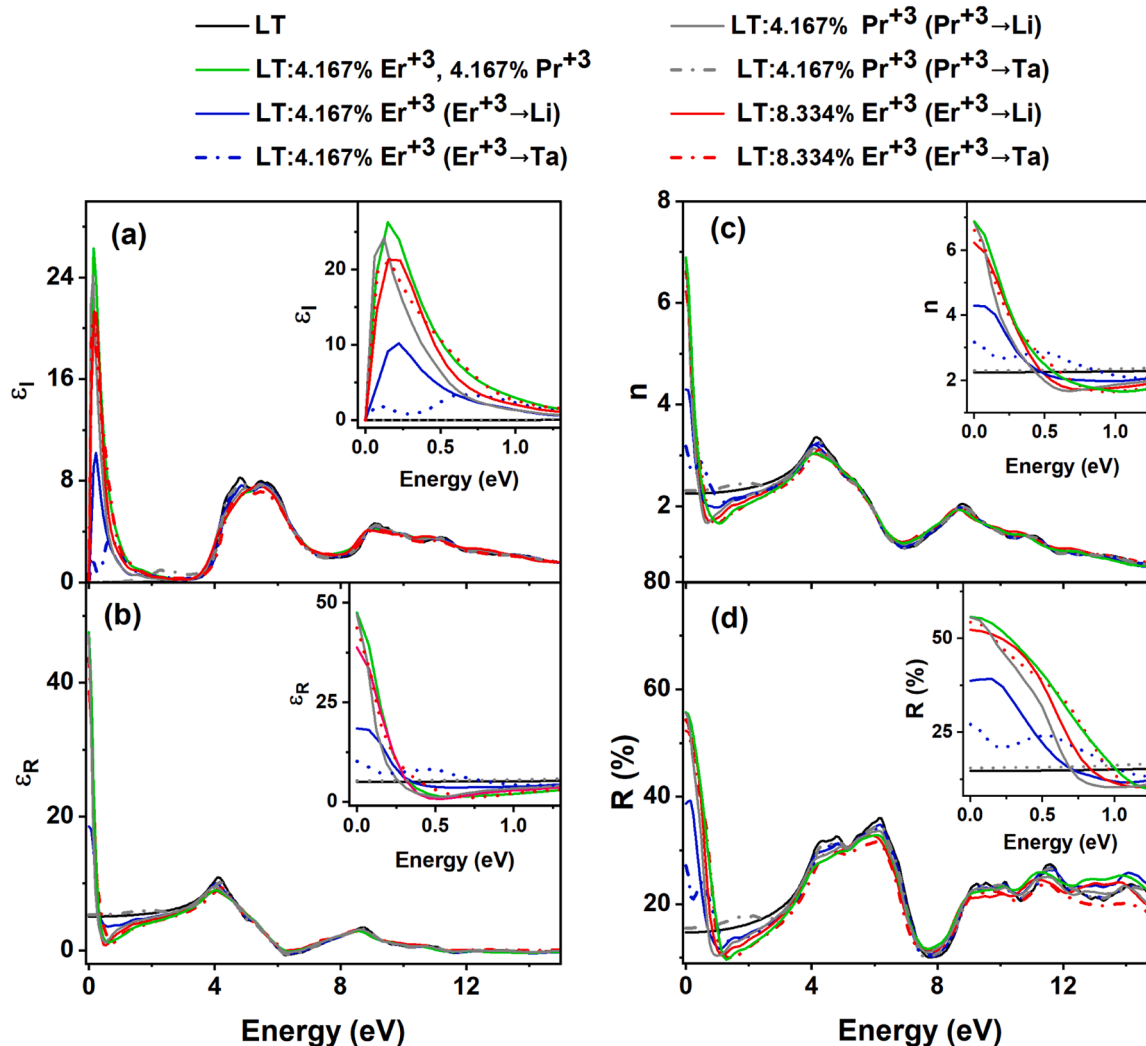


Fig. 5. a) The frequency-dependent imaginary part of dielectric functions  $\epsilon_I$  for LT and its  $\text{Er}^{+3}$  and  $\text{Pr}^{+3}$  doped and co-doped counterparts for  $\text{Er}^{+3}$  and  $\text{Pr}^{+3}$  at the Li site ( $\text{Er}^{+3}$ ,  $\text{Pr}^{+3} \rightarrow \text{Li}$ ) and the Ta site ( $\text{Er}^{+3}$ ,  $\text{Pr}^{+3} \rightarrow \text{Ta}$ ) b) the real part  $\epsilon_R$ , c) the refractive index  $n$ , and d) the reflectivity  $R$ .

We now examine the changes in the  $\epsilon_I$  peaks in the bandgap due to LT doping with  $\text{Er}^{+3}$ . For 8.334 %  $\text{Er}^{+3}$  the  $\epsilon_I$  maxima in the above energy region are about the same, irrespective of the location of the  $\text{Er}^{+3}$  dopant in the LT. However, this is in contrast with the results from LT: 4.167 %  $\text{Er}^{+3}$  where the  $\epsilon_I$  maxima is higher for the case that the dopant is at the Li site relative to the Ta site. Recall that for the  $\text{Er}^{+3}$  at the Li site, the PBE calculations show the 4f orbitals are located at the Fermi energy and in the conduction band bottom, thus allowing mixing with the LT bands. The high  $\epsilon_I$  maxima for LT: 8.334 %  $\text{Er}^{+3}$  with  $\text{Er}^{+3}$  at the Ta site is attributed to the significant broken octahedral symmetry within the  $\text{Er}^{+3}$ -O units, which translates to changes in the  $\text{Er}^{+3}$ -4f bands, as explained in the last subsection.

The dielectric constant  $\epsilon_R(0)$  increases following the trend LT: 4.167 %  $\text{Er}^{+3}$ , 4.167 %  $\text{Pr}^{+3} \approx$  LT:4.167 %  $\text{Pr}^{+3}$  ( $\text{Pr}^{+3} \rightarrow \text{Li}$ ) > LT: 8.334 %  $\text{Er}^{+3}$  ( $\text{Er}^{+3} \rightarrow \text{Ta}$ ) > LT: 8.334 %  $\text{Er}^{+3}$  ( $\text{Er}^{+3} \rightarrow \text{Li}$ ) > LT: 4.167 %  $\text{Er}^{+3}$  ( $\text{Er}^{+3} \rightarrow \text{Li}$ ) > LT: 4.167 %  $\text{Er}^{+3}$  ( $\text{Er}^{+3} \rightarrow \text{Ta}$ ). This same trend applies to the static refractive index  $n(0)$  and the static reflectivity  $R(0)$ . The changes in the  $\epsilon_R(0)$  are indicative that the co-doped configuration and the LT:4.167 %  $\text{Pr}^{+3}$  ( $\text{Pr}^{+3} \rightarrow \text{Li}$ ) are better dielectrics than all other doped configurations here.

It has been reported that there is an inverse relationship between static refractive index  $n(0)$  and the optical bandgap energy [77], whereas Gomaa et al. proposed that  $n(0)$  is proportional to the square root of this bandgap energy. Here, the static refractive indexes are

correlated with f-f intraband transitions, and thus, the higher the  $n(0)$ , the smaller the energy difference between the two 4 f bands. Changes in the static reflectivity due to doping and co-doping are indicative of improved mirror properties in the IR for the co-doping configuration and for the LT:4.167 %  $\text{Pr}^{+3}$  ( $\text{Pr}^{+3} \rightarrow \text{Li}$ ) relative to all other configurations examined here.

#### 3.4. QTAIM analysis, Bader charges, and ELF

Table 2 shows the calculated QTAIM properties for the metal-O bond critical points for LT and LT doped and co-doped with  $\text{Er}^{+3}$  and  $\text{Pr}^{+3}$  of this work. For all cases here,  $|V_b|/G_b < 2$ ,

indicating either closed shell or incipient covalent bonding. Moreover, for LT and its doped and co-doped configurations, the Li-O electron density and its Laplacian at the Li-O bond critical point are significantly smaller than the corresponding Ta-O  $\nabla \rho_b(\vec{r})$  and  $\nabla^2 \rho_b(\vec{r})$ , and indicate weaker Li-O bonding relative to Ta-O. The Li-O interaction is a closed shell for the LT due to  $|V_b|/G_b < 1$  and  $H_b > 0$ , whereas the Ta-O is incipient covalent ( $1 < |V_b|/G_b < 2$  and  $H_b < 0$ ) for all configurations here. The DOS calculations of this work and our previous work [10] showed an overlap between Ta-d and O-sp orbitals, interpreted as strong covalent Ta-O bonding. However, this is in contrast with QTAIM, which does not show strong covalent bonding for metal-O interactions. Therefore, interpretations of orbital overlaps on bonding solely from

**Table 2**

QTAIM parameters at the Li-O, Ta-O, and X-O for  $X = \text{Er}^{+3}$ ,  $\text{Pr}^{+3}$  bond critical points (3, -1; b) and their corresponding interatomic distances for LT, LT:4.167 %  $\text{Er}^{+3}$  and LT:8.334 %  $\text{Er}^{+3}$  with Er located in the Li or the Ta site, and the LT: 4.167 %  $\text{Pr}^{+3}$  and LT: 4.167 %  $\text{Er}^{+3}$ , 4.167 %  $\text{Pr}^{+3}$ , with the dopant atoms in the Li site. Only the QTAIM properties, which correspond to the smaller metal-bond critical point-oxygen distances, are shown for the doped configurations.

Configuration	Distances (Å)	QTAIM properties (a.u.)			
		$\rho(\vec{r}_b)$	$\nabla^2\rho(\vec{r}_b)$	$(H/\rho)(\vec{r}_b)$	$( V/G)(\vec{r}_b)$
	Li-O (Ta-O) [X-O], X = Er, Pr				
LT	2.021 2.312 (1.929) (2.066)	0.024 0.012 (0.154) (0.109)	0.162 0.076 (0.557) (0.403)	0.315 0.370 (-0.518) (-0.345)	0.787 0.690 (1.361) (1.271)
LT:4.167 % $\text{Er}^{+3}$ ( $\text{Er}^{+3} \rightarrow \text{Li}$ )	2.001 (1.927) [2.207]	0.025 (0.155) [0.076]	0.200 (0.453) [0.300]	0.415 (-0.583) [-0.189]	0.736 (1.443) [1.162]
LT: 4.167 % $\text{Er}^{+3}$ ( $\text{Er}^{+3} \rightarrow \text{Ta}$ )	1.968 (1.925) [2.165]	0.028 (0.156) [0.085]	0.174 (0.484) [0.300]	0.252 (-0.573) [-0.259]	0.807 (1.426) [1.227]
LT:8.334 % $\text{Er}^{+3}$ ( $\text{Er}^{+3} \rightarrow \text{Li}$ )	2.009 (1.932) [2.156]	0.025 (0.151) [0.086]	0.060 (0.573) [0.339]	-0.050 (-0.498) [-0.227]	1.078 (1.344) [1.187]
LT:8.334 % $\text{Er}^{+3}$ ( $\text{Er}^{+3} \rightarrow \text{Ta}$ )	1.907 (1.880) [2.150]	0.032 (0.174) [0.088]	0.037 (0.618) [0.307]	-0.196 (-0.601) [-0.275]	1.408 (1.404) [1.239]
LT: 4.167 % $\text{Pr}^{+3}$ ( $\text{Pr}^{+3} \rightarrow \text{Li}$ )	1.996 (1.853) [2.230]	0.027 (0.156) [0.088]	0.164 (0.582) [0.283]	0.284 (-0.527) [-0.306]	0.801 (1.353) [1.278]
LT: 4.167 % $\text{Er}^{+3}$ , 4.167 % $\text{Pr}^{+3}$ ( $\text{Er}^{+3}$ , $\text{Pr}^{+3} \rightarrow \text{Li}$ )	1.991 (1.936)	0.027 (0.151)	0.026 (0.549)	-0.176 (-0.501)	1.420 (1.358)
<sup>a</sup>	[2.225]	[0.073]	[0.306]	[-0.151]	[1.123]
<sup>b</sup>	[2.243]	[0.086]	[0.270]	[-0.296]	[1.274]

<sup>a</sup>  $\text{Er}^{+3}$ -O and

<sup>b</sup>  $\text{Pr}^{+3}$ -O.

results on the DOS could be fortuitous. The same applies to statements about bonding between two atoms using results from charge transfers (vide infra).

For the LT:8.334 %  $\text{Er}^{+3}$  and the co-doped  $\text{Er}^{+3}$ , $\text{Pr}^{+3}$  configuration, the shortest Li-O interaction appears incipient covalent due to the increased coupling between these two atoms' sp orbitals, whereas longer Li-O distances correspond to closed shell interactions. The  $\text{Er}^{+3}$ -O and  $\text{Pr}^{+3}$ -O interactions are incipient covalent, with the  $\text{Pr}^{+3}$ -O distance larger than the  $\text{Er}^{+3}$ -O distance ( $1 < |V_b|/G_b < 2$  and  $H_b < 0$ ; Table 2). These interactions have similar strengths as found by the values of their electron densities at the corresponding bond critical points.

Table 3 shows the atomic charges and volumes for all atoms and configurations of this work. The atomic volume is the Bader region used to calculate the atom charge via integration. For LT, we get  $\text{Li}^{0.87}\text{Ta}^{2.64}\text{O}^{1.17}$ , which agrees with our past calculations using a denser BZ grid. The charge analysis alone indicates that Ta-O interaction is covalent because the calculated Ta charge is less than expected from the chemical formula (i.e.,  $\text{Ta}^{+5}$ ). However, an accurate description of the degree of covalency is from QTAIM, which shows that Ta-O bonding is incipient covalent. Therefore, QTAIM should be employed to describe the bonding between two atoms accurately.

The atomic volumes of  $\text{Er}^{+3}$ ,  $\text{Pr}^{+3}$ , and O are similar, whereas the Ta one is smaller, and the Li one is the smallest. Oxygens are electronegative and were found to exhibit high atomic volumes. Thus, Li, which is electropositive, has the smallest atomic volume. The lanthanides' high volumes could be attributed to including the 4f orbitals in the valence. For the doped and co-doped configurations,  $\text{Er}^{+3}$  and  $\text{Pr}^{+3}$  have charge

**Table 3**

Atomic charges in units of  $e$  and volumes in  $\text{\AA}^3$  for LT, LT:8.334 %  $\text{Er}^{+3}$  and with LT: 4.167 %  $\text{Pr}^{+3}$  the dopant atom in either in the Li or the Ta site, and LT: 4.167 %  $\text{Er}^{+3}$ , 4.167 %  $\text{Pr}^{+3}$ , with the dopant atoms in the Li site.

Configuration	Atomic charges ( $e$ )				
	[Atomic Volumes ( $\text{\AA}^3$ )]				
	Li	Ta	$\text{Er}^{+3}$	$\text{Pr}^{+3}$	O
LT	-0.87	-2.64			1.17
	[3.15]	[9.65]			[13.39]
LT:8.334 % $\text{Er}^{+3}$ ( $\text{Er}^{+3} \rightarrow \text{Li}$ )	-0.88	-2.58	-1.77		1.18
	[3.33]	[10.00]	[12.96]		[13.48]
LT:8.334 % $\text{Er}^{+3}$ ( $\text{Er}^{+3} \rightarrow \text{Ta}$ )	-0.87	-2.61	-2.06		1.15
	[3.18]	[9.83]	[12.82]		[13.61]
LT: 4.167 % $\text{Pr}^{+3}$ ( $\text{Pr} \rightarrow \text{Li}$ )	-0.87	-2.59		-1.97	1.17
	[3.25]	[9.83]		[15.41]	[13.41]
LT: 4.167 % $\text{Pr}^{+3}$ ( $\text{Pr} \rightarrow \text{Ta}$ )	-0.87	-2.62			1.16
	[3.16]	[9.79]		[14.11]	[13.40]
LT: 4.167 % $\text{Er}^{+3}$ , 4.167 % $\text{Pr}^{+3}$ (Er, $\text{Pr} \rightarrow \text{Li}$ )	-0.88	-2.57	-1.70	-1.70	1.18
	[3.30]	[9.89]	[13.59]	[15.63]	[13.42]

decreases relative to the isolated atomic charges between 1.70 and 2.06 for  $\text{Er}^{+3}$  and 1.70–1.97 for  $\text{Pr}^{+3}$ , which are less than what is expected from the chemical formula. This agrees with our past work on LT: 4.167 %  $\text{Er}^{+3}$ . We must state that changes in the  $\text{Er}^{+3}$  and  $\text{Pr}^{+3}$  charges do not affect the strength of the  $\text{Er}^{+3}$ -O and  $\text{Pr}^{+3}$ -O bonds.

Fig. 6 shows the ELF contour maps for the LT: 4.167 %  $\text{Er}^{+3}$ , 4.167 %  $\text{Pr}^{+3}$  unit cell at various planes. The ELF maps for other configurations are similar and thus not reported here. It is observed that ELF is concentrated around the Ta,  $\text{Er}^{+3}$ , and  $\text{Pr}^{+3}$  atoms, whereas ELF is not observed around Li. Recall that only the valence orbitals are included in the pseudopotentials used here. ELF is about zero in the regions between metals and oxygens, which indicates the absence of strong covalent bonding between these atoms. Moreover, the ELF around Ta,  $\text{Er}^{+3}$ , and  $\text{Pr}^{+3}$  atoms is distorted due to a small overlap, in agreement with the incipient covalent bonding formalism from QTAIM results.

#### 4. Conclusions

DFT band structure and DOS calculations under GGA showed that the location of the  $\text{Er}^{+3}$ - and  $\text{Pr}^{+3}$ -4f bands is in the conduction band bottom when  $\text{Er}^{+3}$  and  $\text{Pr}^{+3}$  on the Li site, in the valence band top for the  $\text{Er}^{+3}$  on the Ta site, and in the bandgap when  $\text{Pr}^{+3}$  is on the Ta site. The presence of peaks in the imaginary part of the dielectric function  $\epsilon_I$  in the bandgap indicates f-f intraband transitions. The strength of these transitions is analogous to the  $\epsilon_I$  maxima values in the bandgap. For dopants at the Li site, the f-f transitions are stronger for the LT:  $\text{Pr}^{+3}$  relative to LT:  $\text{Er}^{+3}$  for the same % dopant, which agrees with the increased 4f vacancies between these two atoms. Moreover, for  $\text{Er}^{+3}$  doped configurations with  $\text{Er}^{+3}$  at the Li site, an increased % dopant leads to stronger f-f transitions due to the enhanced mixing of the  $\text{Er}^{+3}$ -4f with the LT bands in the conduction band bottom. The absence of  $\epsilon_I$  peaks in the bandgap for the doped configuration with  $\text{Pr}^{+3}$  at the Ta site agrees with the location of the 4f bands in the bandgap and above the Fermi energy and, thus, unpopulated. In this case, for  $\text{Er}^{+3}$  at the Ta site, structural changes around the  $\text{Er}^{+3}$  atoms distort the  $\text{Er}^{+3}$ -O octahedral symmetry, leading to the broadening and upshifting of the Er-4f bands, thus increasing the 4f vacancies and strengthening the f-f intraband transitions.

Hybrid HSE06 calculations, which are computationally expensive, improve the bandgap's accuracy and the location of the 4f bands.

The QTAIM and ELF show that the Li-O interaction is of a closed shell, whereas Ta-O,  $\text{Er}^{+3}$ -O, and  $\text{Pr}^{+3}$ -O are incipient covalent. The Ta-O bonding classification contrasts the interpretation from results from DOS and charge transfers, where orbital overlap and significant charge transfer were seen as strong covalent interactions. Thus, using QTAIM

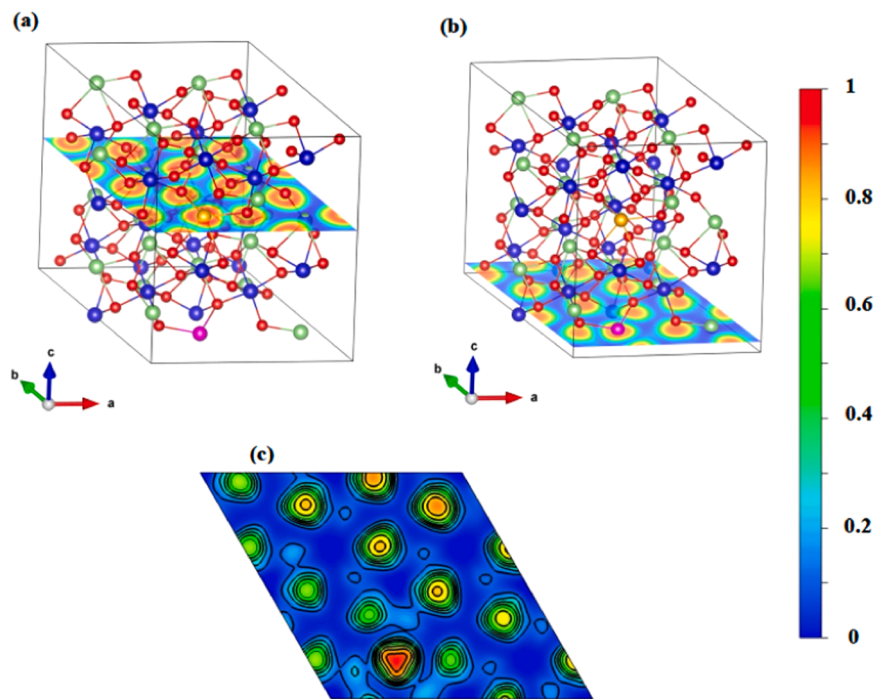


**Fig. 6.** ELF contour maps for the LT: 4.167 % Er<sup>+3</sup>, 4.167 % Pr<sup>+3</sup> unit cell (a) at the plane (001) plane passing through the Er<sup>+3</sup> atom and (b) the Pr<sup>+3</sup> atom. (c) ELF at the plane defined by Pr<sup>+3</sup> and the new nearest O atoms. Red, strong localization (ELF = 1); green free electron gas (ELF = 1/2); blue, no localization (ELF = 0).

and ELF avoids fortuitous statements on bonding between two atoms.

#### CRedit authorship contribution statement

**Tarawneh Constantine M.:** Validation, Resources, Funding acquisition, Data curation. **Bhatti Muhammad I.:** Visualization, Resources, Data curation. **Martirosyan Karen S.:** Validation, Resources, Data curation. **Herrera Yosef:** Writing – original draft, Validation, Formal analysis. **Pelayo Carvajal Andrea:** Writing – review & editing, Validation, Supervision, Data curation. **Dimakis Nicholas:** Writing – review & editing, Writing – original draft, Visualization, Validation, Supervision, Project administration, Methodology, Formal analysis, Data curation, Conceptualization. **Resendez Tianna:** Validation, Formal analysis. **Uddin Mohammed Jasim:** Validation, Resources, Data curation. **Hobosyan Mkhitar A.:** Supervision.

#### Declaration of Competing Interest

The authors declare that they have no known competing financial interests or personal relationships that could have appeared to influence the work reported in this paper.

#### Acknowledgments

The author(s) would like to acknowledge funding provided by the National Science Foundation CREST Center for Multidisciplinary Research Excellence in Cyber-Physical Infrastructure Systems (NSF Award No. 2112650). The opinions expressed in this paper (or thesis report or dissertation) are solely those of the author(s) and do not necessarily represent those of the NSF. The authors also acknowledge the Texas Advanced Computing Center (TACC) at The University of Texas at Austin for providing HPC resources that have contributed to the research results reported within this paper. URL: <http://www.tacc.utexas.edu>.

#### Appendix A. Supporting information

Supplementary data associated with this article can be found in the online version at [doi:10.1016/j.mtcomm.2025.112047](https://doi.org/10.1016/j.mtcomm.2025.112047).

#### Data availability

Data will be made available on request.

#### References

- [1] G. Rose, Beschreibung einiger Neuen Mineralien Des Urals, *Ann. Der Phys.* 124 (1839) 551–573.
- [2] M. Nyman, T.M. Anderson, P.P. Provencio, Comparison of Aqueous and Non-Aqueous Soft-Chemical Syntheses of Lithium Niobate and Lithium Tantalate Powders, *Crystal Growth & Design*, (2008).
- [3] P.P. Phulé, T. Deis, D.G. Dindiger, Low temperature synthesis of ultrafine LiTaO<sub>3</sub> powders, *J. Mater. Res.* (1991).
- [4] S.K. Sahu, S. Zlotnik, A. Navrotsky, P.M. Vilarinho, Thermodynamic stability of lead-free alkali niobate and tantalate perovskites, *J. Mater. Chem. C* (2015).
- [5] F. Akram, A. Hussain, R.A. Malik, T.K. Song, W.-J. Kim, M.-H. Kim, Synthesis and electromechanical properties of LiTaO<sub>3</sub>-modified BiFeO<sub>3</sub>-BaTiO<sub>3</sub> piezoceramics, *Ceram. Int.* (2017).
- [6] H. Ye, S.C. Kumar, J. Wei, P.G. Schunemann, M. Ebrahim-Zadeh, Optical parametric generation in orientation-patterned gallium phosphide, *Opt. Lett.* (2017).
- [7] F. Rotermund, C.-H. Yoon, S. Kurimura, N.-E. Yu, K. Kitamura, V. Petrov, F. Noack, Efficient Optical Parametric Chirped Pulse Amplification at 1 kHz Using Periodically Poled Stoichiometric LiTaO<sub>3</sub>/sub 3, (2005).
- [8] X. Yang, Y. Zhu, D. Ma, S. Long, Z. Liu, B. Wang, Luminescent properties of stoichiometric Er:LiTaO<sub>3</sub> submicron particles synthesized by a modified solid-state combustion route, *Ceram. Int.* 45 (2019) 10733–10739.
- [9] X. Yang, S. Lin, D. Ma, S. Long, Y. Zhu, H. Li, B. Wang, Up-conversion luminescence of LiTaO<sub>3</sub>:Er<sup>3+</sup> phosphors for optical thermometry, *Ceram. Int.* 46 (2020) 1178–1182.
- [10] M.A. Hobosyan, A.P. Carvajal, B.B. Srivastava, T. Zakia, M.J. Uddin, K. S. Martirosyan, E. Rodriguez, K.N. Ackaah-Gyasi, N. Dimakis, Computational and experimental study on undoped and Er-doped lithium tantalate nanofluorescent probes, *Mater. Today Commun.* 36 (2023) 106503.
- [11] G.J. Qiu, H.H. Ye, X.S. Wang, H. Fang, Y.X. Li, X. Yao, Intense piezoluminescence in LiTaO<sub>3</sub> phosphors doped with Pr<sup>3+</sup> ions, *Ceram. Int.* 45 (2019) 8553–8560.
- [12] A. Ismail, S. Subiyanto, S. Sudrajat, W.G. Prakoso, A. Saepulrohman, The effect of cerium doping on LiTaO<sub>3</sub> thin film on band gap energy, *Int. J. Electron. Commun. Syst.* 1 (2021) 63–67.

- [13] Y. Irzaman, E.R. Pebriyanto, I. Apipah, Alkadri A. Noor, Characterization of optical and structural of lanthanum doped LiTaO<sub>3</sub> thin films, *Integr. Ferroelectr.* 167 (2015) 137–145.
- [14] X. Li, R. Hu, X.S. Wang, Y.X. Li, X. Yao, Intense mechanoluminescence and photostimulated luminescence with less afterglow in Pr<sup>3+</sup>/Gd<sup>3+</sup> co-doped LiTaO<sub>3</sub> phosphors, *J. Lumin.* 238 (2021).
- [15] L. Shi, Q. Shen, Z. Qiu, Concentration-dependent upconversion emission in Er-doped and Er/Yb-codoped LiTaO<sub>3</sub> polycrystals, *J. Lumin.* 148 (2014) 94–97.
- [16] D. Ding, W. Ding, R. Huang, Y. Fu, F. Xu, Research progress of laser triangulation on-machine measurement technology for complex surface: a review, *Measurement* 216 (2023) 113001.
- [17] W. Kohn, L.J. Sham, Self-consistent equations including exchange and correlation effects, *Phys. Rev.* 140 (1965) A1133–A1138.
- [18] P. Hohenberg, W. Kohn, Inhomogeneous electron gas, *Phys. Rev.* 136 (1964) B864–B871.
- [19] F. Aryasetiawan, O. Gunnarsson, The GW method, *Rep. Prog. Phys.* 61 (1998) 237–312.
- [20] F. Aryasetiawan, S. Biermann, Generalized Hedin's equations for quantum many-body systems with spin-dependent interactions, *Phys. Rev. Lett.* 100 (2008).
- [21] F. Toksoy, S. Cabuk, DFT - based study of electronic structures and mechanical properties of LiTaO<sub>3</sub>: ferroelectric and paraelectric phases, *Philos. Mag.* 97 (2017) 2469–2483.
- [22] H. Wang, F. Wu, H. Jiang, Electronic band structures of ATaO<sub>3</sub> (A = Li, Na, and K) from first-principles many-body perturbation theory, *J. Phys. Chem. C* 115 (2011) 16180–16186.
- [23] A. Riefer, S. Sanna, W.G. Schmidt, Lithium niobate-tantalate mixed crystals electronic and optical properties calculated from first principles, *Proceedings of ISAF-ECAPD-PFM 2012* (2012) 1–3.
- [24] S. Huband, D.S. Keeble, N. Zhang, A.M. Glazer, A. Bartaszyte, P.A. Thomas, Relationship between the structure and optical properties of lithium tantalate at the zero-birefringence point, *J. Appl. Phys.* 121 (2017) 024102.
- [25] S. Sanna, S. Neufeld, M. Rüsing, G. Berth, A. Zrenner, W.G. Schmidt, Raman scattering efficiency in LiTaO<sub>3</sub> and LiNbO<sub>3</sub> crystals, *Phys. Rev. B* 91 (2015) 224302.
- [26] Ç. Süleyman, M. Amirullah, Urbach rule and optical properties of the LiNbO<sub>3</sub> and LiTaO<sub>3</sub>, *J. Opt. A: Pure Appl. Opt.* 1 (1999) 424.
- [27] M. Wiegel, M.H.J. Emond, E.R. Stobbe, G. Blasse, Luminescence of alkali tantalates and niobates, *J. Phys. Chem. Solids* 55 (1994) 773–778.
- [28] H. Kato, A. Kudo, Water Splitting into H<sub>2</sub> and O<sub>2</sub> on Alkali Tantalate Photocatalysts ATaO<sub>3</sub> (A = Li, Na, and K), *J. Phys. Chem. B* 105 (2001) 4285–4292.
- [29] E.-J. Guo, J. Xing, H.-B. Lu, K.-J. Jin, J. Wen, G.-Z. Yang, Ultraviolet fast-response photoelectric effects in LiTaO<sub>3</sub> single crystal, *J. Phys. D: Appl. Phys.* 43 (2010) 015402.
- [30] K. Teramura, S.-i Okuoka, H. Tsuneoka, T. Shishido, T. Tanaka, Photocatalytic reduction of CO<sub>2</sub> using H<sub>2</sub> as reductant over ATaO<sub>3</sub> photocatalysts (A=Li, Na, K), *Appl. Catal. B: Environ.* 96 (2010) 565–568.
- [31] M. Shishkin, G. Kresse, Implementation and performance of the frequency-dependent GW method within the PAW framework, *Phys. Rev. B* 74 (2006) 035101.
- [32] I. Ait Brahim, N. Bekkioui, M. Tahiri, H. Ez-Zahraouy, Doping effect of chalcogens on electronic and optical properties of perovskite LiNbO<sub>3</sub> compound: Ab initio calculations, *Chem. Phys.* 550 (2021) 111320.
- [33] K.O. Obodo, L.L. Noto, S.J. Mofokeng, C.N.M. Ouma, M. Braun, M.S. Dhlamini, Influence of Tm, Ho and Er dopants on the properties of Yb activated ZnTiO<sub>3</sub> perovskite: a density functional theory insight, *Mater. Res. Express* 5 (2018) 106202.
- [34] R. Bader, *Atoms in Molecules: A Quantum Theory*, Oxford Univ. Press, Oxford, 1990.
- [35] R.F.W. Bader, *Atoms in Molecules*, Wiley Online Library, 1990.
- [36] O.A. Syzgantseva, V. Tognetti, L. Joubert, On the physical nature of halogen bonds: a QTAIM study, *J. Phys. Chem. A* 117 (2013) 8969–8980.
- [37] P.S.V. Kumar, V. Raghavendra, V. Subramanian, Bader's theory of atoms in molecules (AIM) and its applications to chemical bonding, *J. Chem. Sci.* 128 (2016) 1527–1536.
- [38] E. Espinosa, I. Alkorta, J. Elguero, E. Molins, From weak to strong interactions: a comprehensive analysis of the topological and energetic properties of the electron density distribution involving X – H ... F – Y systems, *J. Chem. Phys.* 117 (2002) 5529–5542.
- [39] R.F.W. Bader, H. Essén, The characterization of atomic interactions, *J. Chem. Phys.* 80 (1984) 1943–1960.
- [40] P. Macchi, D.M. Proserpio, A. Sironi, Experimental electron density in a transition metal dimer: metal-metal and metal-ligand bonds, *J. Am. Chem. Soc.* 120 (1998) 13429–13435.
- [41] C. Gatti, Chemical bonding in crystals: new directions, *Z. Krist. Cryst. Mater.* 220 (2005) 399–457.
- [42] P.A. Cox, *New York. The Electronic Structure and Chemistry of Solids*, Oxford University Press, 1987.
- [43] B. Boughoufala, H. Bouafia, B. Sahli, B. Djebour, S. Mokrane, S. Hiadi, B. Abidri, DFT + U and QTAIM studies of elastic, magnetic, bonding, and optoelectronic behaviors of RbUO<sub>3</sub>, *J. Supercond. Nov. Magn.* 32 (2019) 4005–4020.
- [44] A.D. Becke, K.E. Edgecombe, A simple measure of electron localization in atomic and molecular systems, *J. Chem. Phys.* 92 (1990) 5397–5403.
- [45] D.B. Chesnut, A. Savin, The electron localization function (ELF) description of the PO bond in phosphine oxide, *J. Am. Chem. Soc.* 121 (1999) 2335–2336.
- [46] M. Jabłoński, M. Palusiak, Basis set and method dependence in atoms in molecules calculations, *J. Phys. Chem. A* 114 (2010) 2240–2244.
- [47] P. Fuentealba, E. Chamorro, J.C. Santos, Understanding and using the electron localization function, in: A. Toro-Labbé (Ed.), *Theor. Comput. Chem.* (2007) 57–85.
- [48] X. Feng, B. Liu, Y. Peng, C. Gu, X. Bai, M. Long, M. Cai, C. Tong, L. Han, J. Yang, Restricting the formation of Pb–Pb dimer via surface Pb site passivation for enhancing the light stability of perovskite, *Small* 18 (2022) 2201831.
- [49] Y.-W. Fang, H. Chen, Design of a multifunctional polar metal via first-principles high-throughput structure screening, *Commun. Mater.* 1 (2020) 1.
- [50] M.A. Hobosyan, A.P. Carvajal, B.B. Srivastava, T. Zakia, M.J. Uddin, K. S. Martirosyan, E. Rodriguez, K.N. Ackaah-Gyasi, N. Dimakis, Corrigendum to “Computational and experimental study on undoped and Er-doped lithium tantalate nanofluorescent probes” [*Mater. Today Commun.* 36 (2023) 106503], *Mater. Today Commun.* 40 (2024) 110032.
- [51] M.A. Hobosyan, A.P. Carvajal, B.B. Srivastava, T. Zakia, M.J. Uddin, K. S. Martirosyan, E. Rodriguez, K.N. Ackaah-Gyasi, N. Dimakis, Computational and experimental data for undoped and Er-doped lithium tantalate nanofluorescent probes, *Data Brief.* 56 (2024) 110771.
- [52] G. Kresse, J. Hafner, Ab initio molecular dynamics for liquid metals, *Phys. Rev. B* 47 (1993) 558(R)–561(R).
- [53] G. Kresse, J. Hafner, Ab initio molecular-dynamics simulation of the liquid-metal–amorphous-semiconductor transition in germanium, *Phys. Rev. B* 49 (1994) 14251–14269.
- [54] G. Kresse, J. Furthmüller, Efficiency of ab-initio total energy calculations for metals and semiconductors using a plane-wave basis set, *Comput. Mater. Sci.* 6 (1996) 15–50.
- [55] G. Kresse, J. Furthmüller, Efficient iterative schemes for ab initio total-energy calculations using a plane-wave basis set, *Phys. Rev. B* 54 (1996) 11169–11186.
- [56] J.P. Perdew, K. Burke, M. Ernzerhof, Generalized gradient approximation made simple, *Phys. Rev. Lett.* 77 (1996) 3865.
- [57] G. Kresse, D. Joubert, From ultrasoft pseudopotentials to the projector augmented-wave method, *Phys. Rev. B* 59 (1999) 1758–1775.
- [58] P.E. Blöchl, Projector augmented-wave method, *Phys. Rev. B* 50 (1994) 17953–17979.
- [59] S. Grimme, J. Antony, S. Ehrlich, H. Krieg, A consistent and accurate ab initio parametrization of density functional dispersion correction (DFT-D) for the 94 elements H-Pu, *J. Chem. Phys.* 132 (2010) 154104–154119.
- [60] A.V. Krukau, O.A. Vydrov, A.F. Izmaylov, G.E. Scuseria, Influence of the exchange screening parameter on the performance of screened hybrid functionals, *J. Chem. Phys.* 125 (2006) 224106, 224105.
- [61] W. Kohn, L.J. Sham, Self-consistent equations including exchange and correlation effects, *Phys. Rev.* 140 (1965) A1133.
- [62] A.J. Garza, G.E. Scuseria, Predicting band gaps with hybrid density functionals, *J. Phys. Chem. Lett.* 7 (2016) 4165–4170.
- [63] P. Hohenberg, W. Kohn, Inhomogeneous electron gas, *Phys. Rev.* 136 (1964) B864.
- [64] J. Heyd, G.E. Scuseria, M. Ernzerhof, Hybrid functionals based on a screened Coulomb potential, *J. Chem. Phys.* 118 (2003) 8207–8215.
- [65] W. Tang, E. Sanville, G. Henkelman, A grid-based Bader analysis algorithm without lattice bias, *J. Phys. Condens. Matter* 21 (2009) 084204.
- [66] E. Sanville, S.D. Kenny, R. Smith, G. Henkelman, Improved grid-based algorithm for Bader charge allocation, *J. Comput. Chem.* 28 (2007) 899–908.
- [67] G. Henkelman, A. Arnaldsson, H. Jónsson, A fast and robust algorithm for Bader decomposition of charge density, *Comput. Mater. Sci.* 36 (2006) 354–360.
- [68] M. Yu, D.R. Trinkle, Accurate and efficient algorithm for Bader charge integration, *J. Chem. Phys.* 134 (2011) 064111.
- [69] A. Delin, P. Ravindran, O. Eriksson, J.M. Wills, Full-potential optical calculations of lead chalcogenides, *Int. J. Quantum Chem.* 69 (1998) 349–358.
- [70] A. Otero-de-la-Roza, E.R. Johnson, A.M. Pendás, V. Luña, Critic: a new program for the topological analysis of solid-state electron densities, *Comput. Phys. Commun.* 180 (2009) 1007–1018.
- [71] A. Otero-de-la-Roza, E.R. Johnson, V. Luña, Critic2: a program for real-space analysis of quantum chemical interactions in solids, *Comput. Phys. Commun.* 185 (2014) 1007–1018.
- [72] Y. Aray, J. Rodriguez, Study of CO adsorption on the Fe (100) surface using the Laplacian of the electronic charge density, *Surf. Sci.* 405 (1998) L532–L541.
- [73] D. Vega, D. Almeida, AIM-UC: an application for QTAIM analysis, *J. Comput. Methods Sci. Eng.* 14 (2014) 131–136.
- [74] H. Bethe, Termaufspaltung in Kristallen, *Ann. Phys.* 395 (1929) 133–208.
- [75] F.-N. Wu, H.-J. Yu, Y.-Y. Hu, H.-D. Zhang, R. Zhang, J. Li, B. Liu, X.-P. Wang, Y.-G. Yang, L. Wei, Effects of slight structural distortion on the luminescence performance in (Ca<sub>1-x</sub>Eu<sub>x</sub>)WO<sub>4</sub> luminescent materials, *Luminescence* 36 (2021) 237–246.
- [76] S.L. Adler, Quantum theory of the dielectric constant in real solids, *Phys. Rev.* 126 (1962) 413–420.
- [77] R. Ravichandran, A.X. Wang, J.F. Wager, Solid state dielectric screening versus band gap trends and implications, *Opt. Mater.* 60 (2016) 181–187.